

The Physical Truth Behind the Long-Term Variation of Travel-Time Shifts of Helioseismic Far-Side Images

Grace Y. Jiang

Lynbrook High School

San Jose, CA 95129

Research Mentor:

Dr. Junwei Zhao

W. W. Hansen Experimental Physics Laboratory

Stanford University

Stanford, CA 94305-4085, USA

Abstract

The time-distance helioseismic far-side imaging technique has made it possible to monitor the Sun's magnetic regions and detect far-side ARs by using multiple multi-skip acoustic waves. When the measurement procedure is applied to more than 8000 Sun's far-side images obtained over an 11-year period, it can be used to study the long-term variation of travel-time shifts, which show a very strong anti-correlation with the Sun's global-scale magnetic activities. In this paper, based on the helioseismic imaging model, I design advanced algorithms to compute various surface reflection points according to 14 different schemes, and analyze computational results to investigate three different physical causes that would possibly dominate the long-term travel-time variation. My analysis demonstrates that the acoustic waves that are used for mapping the Sun's far side experience surface reflections around the globe, where they may interact with surface magnetic fields and carry travel-time deficits with them. The mean far-side travel-time shifts from these acoustic waves therefore vary commensurately with the Sun's global magnetic activities.

1 Introduction and Problem Statement:

1.1 Time-Distance Helioseismic Far-side Imaging Technique

Imaging the Sun's active regions (ARs) is useful for modeling the global-scale magnetic fields around the Sun and for predicting the arrival of major ARs that rotate around the limb onto the near side, i.e., the Earth side. Modeling requires inputs from both the near side and the far side of the Sun, but the bulk of the Sun makes the active regions on the Sun's far side not being directly visible to Earth. Consequently, the far-side magnetic fields that are used in most models typically have to rely on observations from days earlier or calculations from some models [Schrijver & DeRosa 2003; Upton & Hathaway 2014].

The Sun's surface continually oscillates. This up-and-down oscillation translates to sound (or acoustic) waves, also called *helioseismic waves*. At each location on the Sun, the motion of these waves will leave a Doppler-shift effect, through the observation of which we can study the Sun's structure and dynamics. The Sun's helioseismic waves, mostly p-mode (or acoustic) waves, can travel and propagate through the Sun's *interior* while reflecting on the Sun's surface. If these waves hit magnetic regions, or ARs, during the travel, they will exhibit travel-time deficits that are generally believed due to the *Wilson depression* [Lindsey, Cally, and Rempel, 2010]. For example, in Figure 1, the lower half of the circle represents the near side of the Sun, and the upper half represents the far side, with the observer situated toward the bottom of the page. Helioseismic waves initiate from the near side of the Sun. The waves propagate through the Sun's *interior* toward the far-side target point. If there exists an AR on the far-side target point, then these waves will experience travel-time deficits. After a couple of continuous reflections, these waves bring the far-side deficit information back to the near side.

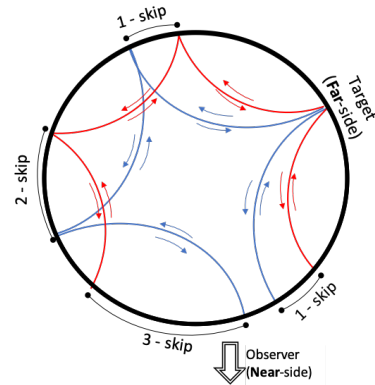


Figure 1 : Travelling of Sun's helioseismic waves. The scheme is named as 1x3-lower which will be explained later.

Most large far-side ARs are detectable through an analysis of such acoustic waves observed on the near side. Zhao et al. [2007] and Ilonidis et al. [2009] have developed and validated a *time-distance helioseismic far-side imaging technique* to image the Sun's far-side ARs using 3-, 4-, and 5- skip helioseismic waves. Figure 1 shows a 4-skip 1x3 scheme, with helioseismic waves starting from the near-side, having one reflection and three reflections on either side of the (far-side) target, respectively. Later, using SDO/HMI Doppler observations [NASA SDO/HMI], Zhao et al. [2019] completely refined the imaging technique to

combine 14 measurement schemes that utilized more types of multi-skip waves, i.e., consisting of 3-, 4-, 5-, 6-, and 8- skips, to detect far-side ARs.

1.2 Objective: Study the Long-Term Variation of Travel-Time Shift

Apart from monitoring the Sun's magnetic activities and detecting active regions (ARs), the *helioseismic far-side imaging technique* can also be used to study the long-term variation of travel-time shifts, or *deficits*, of acoustic waves.

Commissioned on May 01, 2010, the NASA SDO/HMI instrument has been running for over 11 years [NASA SDO/HMI]. It has captured in total more than 8000 helioseismic far-side images with two images every day, obtained at the time 00:00 UT and 12:00 UT of the day. These images are measured maps of acoustic travel-time shifts, relative to the Sun's activity minimum years (2018.01.01 ~ 2019.12.31 for this study). There are dark patches in these images, bearing the meaning of negative travel-time shifts that indicate where ARs are [Stanford JSOC].

Analyzing these 8000+ images will help study the long-term temporal evolution of the travel-time shifts over the 11-year period. We use a longitude-sin(latitude) coordinate system to map the Sun and set the entire far-side longitude to span 180° as $[-90^\circ, +90^\circ]$, and the latitude to span 120° as $[-60^\circ, +60^\circ]$. We adopt a low spatial resolution to define a pixel as $0.8^\circ \times 0.8^\circ$, and calculate the averaged travel-time shift for each pixel over the 11 years. Following that, we average the travel-time shift measurements for all pixels throughout the entirely-defined far-side area, and call the averaged values δ_τ hereafter. Figure 2 shows the long-term variation of the δ_τ over the 11-year time period, where δ_τ is the 90-day running average computed from the Sun's far side disk as well as from the (far-side) northern and southern hemispheres, respectively. The graph clearly shows that both the far-side disk area and the northern and southern parts exhibit a similar long-term trend.

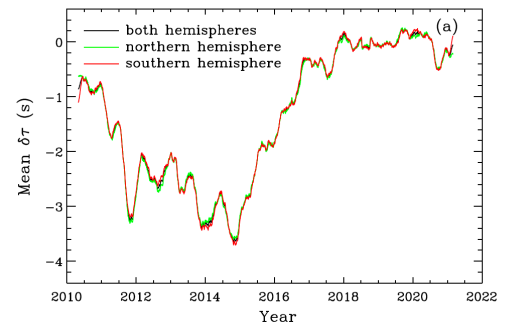


Figure 2 Long-term variation of travel-time shift averaged from Sun's far-side disk, as well as from both northern and southern hemispheres.

We further define another variable, the mean magnetic-flux density, $|B|$, by computing the total absolute value of the near-side full-disk magnetic field and then averaging the sum over the whole near-side spherical area. Figure 3 shows the 90-day running averages¹ of both $|B|$ and $\delta\tau$. Evidently the graph shows a very good anti-correlation, -0.995, between these two quantities, i.e., the travel-time shift and the magnetic flux of the Sun's surface magnetic field.

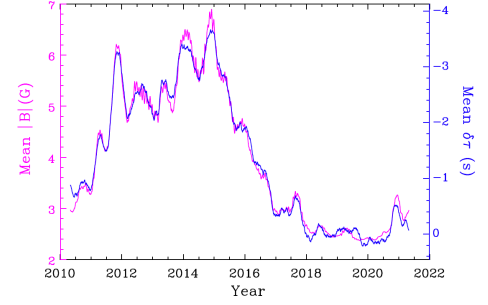


Figure 3 Long-term evolution of the Sun's near-side mean magnetic flux density $|B|$ and far-side mean travel-time shifts $\delta\tau$. Note that the axis for $\delta\tau$ is plotted oppositely.

It is actually not surprising that $\delta\tau$ has a very good anti-correlation with magnetic activity, because the travel-time deficits on far-side maps are mostly caused by the far-side magnetic regions, and the mean far-side magnetic-flux density is not expected to differ much from that of the near side, particularly after a 90-day running average. But, what I want to explore is whether the contributions of far-side magnetic regions are the primary cause of the general variation trend of $\delta\tau$. I believe the *time-distance helioseismic far-side imaging technique* that has been fully developed by Zhao et al. [2007; 2019] has advantages in evaluating the variations.

In this paper, I elucidate the helioseismic far-side imaging technique, examine the long-term variation of travel-time shifts based on time-distance far-side images measured from the *Solar Dynamics Observatory / Helioseismic and Magnetic Imager* [NASA SDO/HMI] observations, and investigate the true physical reason for the variation. I present the modeling & setting of my computation for the time-distance helioseismic far-side imaging codes in section 2 and the detailed algorithm design for calculating both in-skip and final-skip surface reflection points for all multi-skip schemes in section 3. I do data inference and result analysis in section 4 and give conclusion and future consideration in section 5.

2 Modeling Multi-skip Helioseismic Imaging Schemes

Zhao *et al.* [2007; 2019] and Ilonidis et al. [2009] have validated that, for the time-distance helioseismic imaging technique, applying different number of wave-skips to generate far-side images has advantages upon evaluating the measured acoustic travel-time shift (or *deficit*). They have systematically developed imaging codes that include a total of 14 sets of measurement schemes, consisting of 3-, 4-, 5-, 6- and 8-

¹ Since the Sun rotates once in about 27 days, using a 90-day running average over the near-side will actually compute the magnetic field data from the full 360° of the Sun, including both the near and the far sides.

skip helioseismic waves. These codes provide substantial achievements in mapping both existing ARs and rapidly emerging new ARs on the far-side.

2.1 Multi-skip Imaging Scheme with Two Branches

The reflection of helioseismic waves for each measurement scheme consists of two directions, or *branches*, over either side of a target point. Here, I use as an example the 4-skip 2x2 scenario to explain the multi-skip helioseismic far-side imaging scheme. As shown in Figure 4, a far-side target point is at the top of the Sun's great circle. Then, for a total 4-skip wave, if the wave starts from the near side, reflects twice before reaching the far-side target point, and continuously gets reflected twice before traveling back to the near side, then this measurement scheme is called 2x2-*lower* if the total travel distance of the wave is less than 360° (both red and blue waves in Figure 4(a)), or 2x2-*upper* if greater than 360° (only showing one in Figure 4(b)). Hereafter 1° represents 1 degree in the great-circle distance on the solar surface. Evidently, when acoustic waves reflect various times on either side of the mapped far-side locations, they can span the entire area from the Sun's far-side disk center.

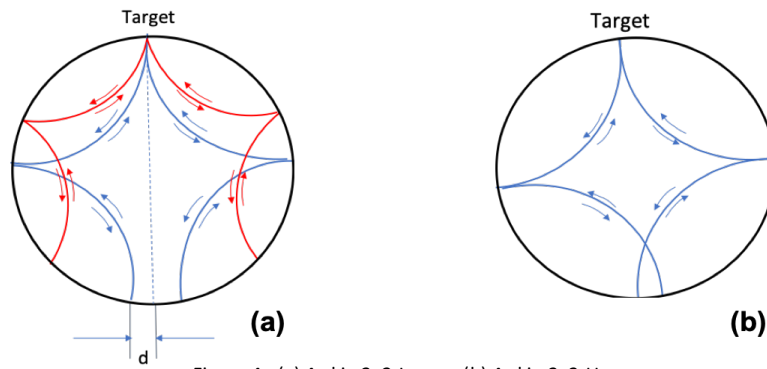


Figure 4 : (a) 4-skip 2x2-Lower; (b) 4-skip 2x2-Upper

Note that while the 4-skip 2x2 -lower and -upper schemes show symmetric reflections on both directions of the (far-side) target point, there are other 4-skip schemes bearing asymmetric wave reflections over either direction, like the 4-skip 1x3-lower scheme shown in Figure 1 in section 1.1.

Table 1 shows parameters for all 14 measurement schemes [Zhao, et al. 2019]. All of them have similar two-branch multi-skip reflections. Because helioseismic waves may be subject to different travel-distances (in term of degree), the shortest and longest waves will produce an annulus on their *final* touching points on the Sun's surface. The two-branch directions generate two annuli, e.g., annulus 1 and

2 in the table. Note that for symmetric multi-skip schemes, like 2x2, 3x3, 4x4, etc., their two annuli are actually congruent.

Table 1: Multi-skip helioseismic imaging schemes

Schemes	Annulus 1 Range	Annulus 2 Range
3-skip 1 x 2 lower	96.5° ~ 108.5°	193.0° ~ 217.0°
4-skip 2 x 2 lower	139.8° ~ 172.2°	139.8° ~ 172.2°
4-skip 2 x 2 upper	187.8° ~ 207.0°	187.8° ~ 207.0°
4-skip 1 x 3 lower	69.3° ~ 85.5°	207.9° ~ 256.5°
4-skip 1 x 3 upper	93.5° ~ 105.5°	280.5° ~ 316.5°
5-skip 2 x 3 lower	110.0° ~ 134.0°	165.0° ~ 201.0°
5-skip 2 x 3 upper	150.0° ~ 175.2°	225.0° ~ 262.8°
6-skip 2 x 4 lower	99.5° ~ 110.3°	119.0° ~ 220.6°
6-skip 3 x 3 lower	147.0° ~ 171.0°	147.0° ~ 171.0°
6-skip 3 x 3 upper	189.0° ~ 219.0°	189.0° ~ 219.0°
8-skip 4 x 4 lower	153.0° ~ 171.0°	153.0° ~ 171.0°
8-skip 4 x 4 upper	187.8° ~ 215.4°	187.8° ~ 215.4°
8-skip 2 x 6 lower	73.5° ~ 94.5°	220.5° ~ 283.5°
8-skip 2 x 6 upper	93.5° ~ 102.5°	280.5° ~ 307.5°

2.2 Incompleteness of the Current Multi-skip Imaging Schemes

So far, the multi-skip methods are focusing on investigating surface points that are generated by the *final* reflection locations of helioseismic waves. For example, in Figure 1, waves starting from the Sun’s near-side experience a 1-skip travel to reach the far-side target, after which the waves continue travelling 1 skip and 2 skips on the far side (as marked in the figure), and come back to the near side as the final 3-skip waves. Unfortunately, in current schemes, only oscillatory signals (or *helioseismic waves*) observed in the near-side 1-skip (marked toward the right of the far-side target in Figure 1) and 3-skip annuli (marked toward the bottom in Figure 1) are used to measure travel-time shifts corresponding to the far-side target.

Actually, for the scheme in Figure 1, all waves travel 4 skips in total and touch the surface 5 times. It is obvious that each touch of the surface from these intermediary reflection points will have a possibility of encountering an active region. So, ARs in intermediary locations will also contribute to the time-distance deficits that would be carried along with the waves. We project that exploring them would help understand the physical truth behind the long-term variation of the travel-time shifts.

3 Advanced Algorithms for Calculating Multi-skip Reflection Points

3.1 Computation Modeling & Settings:

3.1.1 A Spherical “3D Sun” Model:

As shown in Figure 5, the Sun is modeled as a 3D sphere. I use a longitude-sin(latitude) coordinate system. Both the near side (the red semi-sphere) and the far-side (the blue semi-sphere) have the latitude range $[-90^\circ, +90^\circ]$, while the longitude range of far-side is $[-90^\circ, +90^\circ]$ and that for near-side is $[+90^\circ, +270^\circ]$. *Target points* are locations on the far side of the Sun that I want to map. Note that the latitude of a (far-side) *target point* is only within the range $[-60^\circ, +60^\circ]$ in my computation. The arcs and their associated arrows on the 3D-Sun show various surface reflections of a multi-skip scheme. This figure demonstrates the mapping of a target point using the 2x2-lower scheme (refer to Table 1).

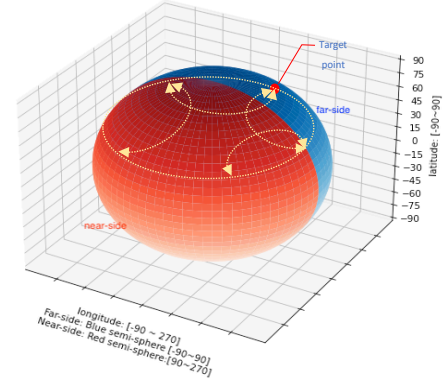


Figure 5 : The spherical 3D-Sun Model

3.1.2 Computation via Spherical Geometry

For a far-side target point (λ, θ) , where λ is latitude and θ is longitude, my objective is to use spherical geometry to calculate all the surface reflection locations, including both in-skip and final-skip points on a great circle. However, for any specific multi-skip scheme, a target point can form numerous great circles that would lead to the generation of hundreds of thousands of reflection points. If I conduct the computation by selecting points from the sphere, then I will have to search the global Sun for every far-side target-point (because in-skip locations could fall on either far-side or near-side semi-sphere). Remember that target-points are distributed around the most far-side area, and I have 14 multi-skip schemes (see Table 1). Consequently, this process shall produce billions of 3D-geometric computations, which make the whole process extremely computationally complex.

Therefore, I devised a much more efficient solution by utilizing the corresponding *antipode* (on the near-side) of a far-side target point. For a target point (λ, θ) , the coordinate of its antipode is given by $(-\lambda, \theta+180^\circ)$. Then, the final-skip locations would reside on a round circling the antipode. The computation procedure consists of 2 steps:

- 1) The antipode is designated as the circle-center. I derive the radius d of the circle from the skip-distance of a multi-skip scheme, and conduct an exhaustive searching to find all the *final* reflection points that have the spherical distance d from the antipode. The searching spatial-resolution is set at $0.8^\circ \times 0.8^\circ$ pixel⁻¹.

2) Thanks to the requirements in section 3.1.4, once the final reflection points are found, I apply algorithms, which are designed to deal with different multi-skip schemes as in Table 1, to compute all the in-skip reflection points. The details of these algorithms are explained in section 3.2.

Here, I use the 4-skip 2x2-lower scheme to explain the procedure. In Figure 6, the far-side target is at $(\lambda=0^\circ, \theta=0^\circ)$, noted as the blue dot, and its antipode is $(\lambda=0^\circ, \theta=180^\circ)$, noted as the red dot. From Table 1, the lowest value of the annulus-1 is 139.8° . Since there are 2 skips on a branch, the one-skip distance (in degrees) would be $139.8^\circ/2=69.9^\circ$. From Figure 4(a), I can derive the radius d of the circle, $d = (180^\circ - 69.9^\circ \times 2) = 40.2^\circ$. Then, I search exhaustively to find all the 2-skip (i.e., the final-skip) reflection locations shown as the small (right) circle in the figure. The big (left) circle forms the 1-skip (i.e., in-skip) reflection points that are computed based on algorithms in section 3.2.

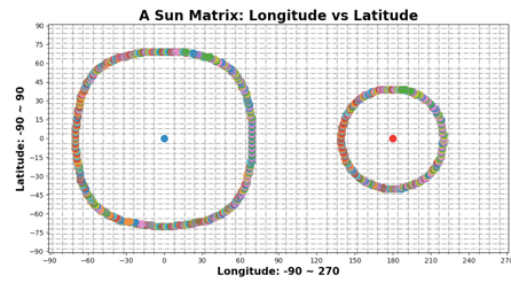


Figure 6 : 4-skip 2x2-lower computation results

3.1.3 Possibly Biased Computation on a Circle:

Unfortunately, the exhaustive searching itself bears an intrinsic shortcoming if some part of a circle is close to a high-latitude section, especially around the northern or the southern poles, where the results experience an extremely biased distribution. For example, suppose a far-side target point is at $(\lambda = -50^\circ, \theta = 0^\circ)$, and its corresponding antipode is thus at $(\lambda = +50^\circ, \theta = 180^\circ)$. From the 4-skip 2x2-lower scheme with one-skip distance 69.9° , Figure 7 shows the 2nd-skip (i.e., the final-skip) “circle” on the near-side, clustering around the northern pole (latitude= 90°) where the longitude would be $90^\circ \sim 270^\circ$ (for whole near-side only). For the points on the straight line in the figure, they are actually the same point (all being the north pole)! As a not uncommon scenario, this type of near-polar bias will result in a significant disruption to my computation.

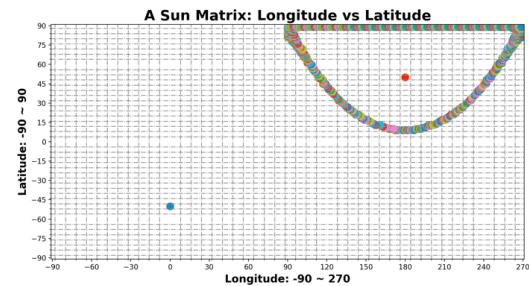


Figure 7 : Biased around polar area (4-skip 2x2-lower)

Therefore, I had to apply an elimination algorithm to remove this cluster of biased points.

3.1.4 A Critical Requirement: Mapping 1-to-1 Among In-skip and Final Reflection Points

I must emphasize that, for a given target point, the algorithm applied in the 2nd-step of the computation (in section 3.1.2) must guarantee a 1-to-1 mapping between the final-skip points and all its corresponding in-skip points belonging to the same scheme. For example, in the 1x3-lower case (Figure 1), let's imagine a small particle initiates from the far-side target point. Then, toward the 3-skip branch, it will reflect first

on the Sun's surface as the 1st in-skip, second on the surface as the 2nd in-skip, and finally land on the surface as the final-skip location. In reality, these three reflection points are related to each other and will stay on the same great-circle plane. Thus, they must be computed as a whole to maintain a 1-to-1 mapping among them. However, if the exhaustive searching from section 3.1.2 is separately conducted for in-skip and final-skip points, then their independent computations cannot guarantee the required 1-to-1 mapping. So, I design the following advanced algorithms to address the challenge.

3.2 Advanced Algorithms for 1-to-1 In-skip Computation

Hereafter in this section, I always use λ to denote latitude and θ as longitude under the longitude-sin(latitude) coordinate system. The coordinate of a point is (latitude, longitude) = (λ, θ) .

3.2.1 Points & Vectors Conversion:

My spherical computation needs to convert between a point (λ, θ) and its corresponding 3D vector, i.e., $(\lambda, \theta) \leftrightarrow V(x, y, z)$, where x, y, z corresponds to 3 axes of the 3D cartesian coordinate. For the 3D-Sun model in Figure 5, the positive x -axis points from the Sun's center toward the far-side, the positive y -axis toward the right-side and the positive z -axis points upward. Let's consider a unit sphere $\|V\| = \sqrt{x^2 + y^2 + z^2} = 1$, then the following known formula shows the corresponding conversions:

- Point to Vector conversion: $(\lambda, \theta) \rightarrow V(x, y, z)$

$$\begin{cases} x = \cos\lambda * \cos\theta \\ y = \cos\lambda * \sin\theta \\ z = \sin\lambda \end{cases}$$

- Vector to Point conversion: $V(x, y, z) \rightarrow (\lambda, \theta)$

$$\begin{cases} \lambda = \arcsin(z) \\ \theta = \text{atan2}(y, x) \end{cases} \quad \text{where } \text{atan2}(y, x) = \begin{cases} \arctan\left(\frac{y}{x}\right) & \text{if } x > 0 \\ \arctan\left(\frac{y}{x}\right) + \pi & \text{if } x < 0 \text{ and } y \geq 0 \\ \arctan\left(\frac{y}{x}\right) - \pi & \text{if } x < 0 \text{ and } y < 0 \\ +\frac{\pi}{2} & \text{if } x = 0 \text{ and } y > 0 \\ -\frac{\pi}{2} & \text{if } x = 0 \text{ and } y < 0 \\ \text{undefined} & \text{if } x = 0 \text{ and } y = 0 \end{cases}$$

Note that the range of the function, $\text{atan2}(a, b)$, is $(-\pi, +\pi)$, while in my longitude-sin(latitude) coordinate system (as in section 3.1.1), the range of longitude θ is $(-\frac{\pi}{2}, +\frac{3\pi}{2})$. Fortunately, this discrepancy occurs only in the case $\{x < 0 \text{ \& } y < 0\}$, shown as the shaded area in Figure 8. For this specific scenario, I just need to add 2π to map the common $\text{atan2}()$ function to my coordinate setting.

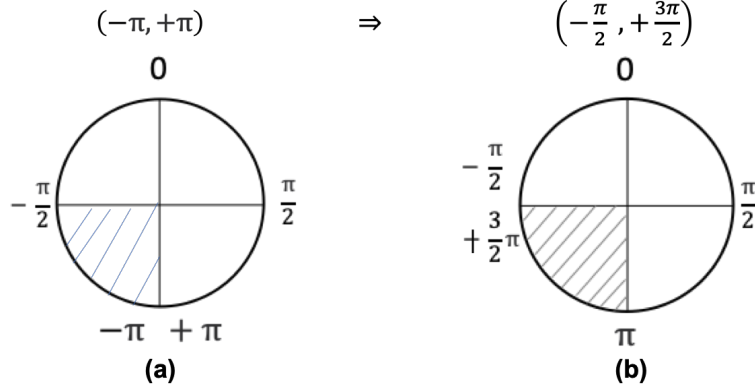


Figure 8 : (a) Normal range of function atan2(); (b) New range in my coordinate system with 3rd-quadrant re-mapping

Table 1 shows 14 different schemes with various multiple skips in each branch, like 2, 3, 4 and 6. Depending on the annulus range of a scheme, the algorithm to calculate all its in-skip locations may vary. Therefore, I will categorize them to explain.

3.2.2 Find the Mid-point via Spherical Geometry

Some schemes in Table 1 have a branch with 2 skips, e.g., 2x2-lower, 2x3-upper, etc., Then, for a given far-side target point (T), after a final-skip point (F) is found via exhaustive searching, I compute the mid-point M (as the 1st in-skip location) between them. As shown in Figure 9, suppose the center of the corresponding great circle is O , then based on the angle α formed between vectors \overrightarrow{OT} and \overrightarrow{OF} , I can categorize the computation into two cases, i.e., $\alpha < 180^\circ$ and $\alpha > 180^\circ$. Note that the computation for $\alpha=180^\circ$ can be easily handled as a special case. So, I will not list it in all of the following scenarios.

1) Case-1: $\alpha < 180^\circ$

Suppose the latitude and longitude coordinates of two points are (λ_k, θ_k) , $k = 1, 2$. I consider working on a unit sphere ($\|V_1\| = \|V_2\| = 1$), though the normalization process will make it no significant. Then, according to section 3.2.1, I have

$$V_1 = \begin{bmatrix} \cos \lambda_1 * \cos \theta_1 \\ \cos \lambda_1 * \sin \theta_1 \\ \sin \lambda_1 \end{bmatrix} \quad V_2 = \begin{bmatrix} \cos \lambda_2 * \cos \theta_2 \\ \cos \lambda_2 * \sin \theta_2 \\ \sin \lambda_2 \end{bmatrix}$$

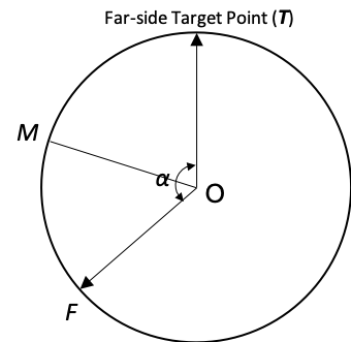


Figure 9 : Mid-point, $\alpha < 180$

Let $V_3 = V_1 + V_2$. With normalization, I have $V_4 = \frac{V_3}{\|V_3\|}$. If the spherical coordinates of V_4 out of its cartesian coordinates is (x, y, z) , it suffices to derive its longitude-sin(latitude) coordinate:

$$\begin{cases} \lambda = \arcsin(z) \\ \theta = \text{atan2}(y, x) \end{cases}$$

Basically, V_3 is the addition of two unit-vectors V_1 and V_2 . Suppose $V_1 = \overrightarrow{OT}$, and $V_2 = \overrightarrow{OF}$, then V_3 will point in the direction of their mid-point M . The vector V_4 is normalized from V_3 , and lies on the unit sphere. As the result, V_4 becomes the projection of the mid-point M (of the target T and the final-skip location F) on the same great-circle plane.

2) Case-2: $\alpha > 180^\circ$

There are schemes in Table 1 for which the vector of a final-skip point (F) will form an angle with the vector of the target far-side point (T) that is greater than 180° . For example, in the 2x2-upper case, the annulus range is 187.8° to 207.0° , indicating $\alpha > 180^\circ$. For this scenario as in Figure 10, using previous algorithm will only derive the opposite mid-point M' , instead of the correct mid-point M .

Thus, my algorithm consists of 3 steps:

- Get the other side of the angle α , which is $(360^\circ - \alpha) < 180^\circ$;
- Apply the algorithm from the above case-1, derive the opposite mid-point $M'(\lambda, \theta)$;
- Since the real mid-point M is the antipode point of M' , then the longitude-sin(latitude) coordinate of M would be $(-\lambda, \theta+180^\circ)$.

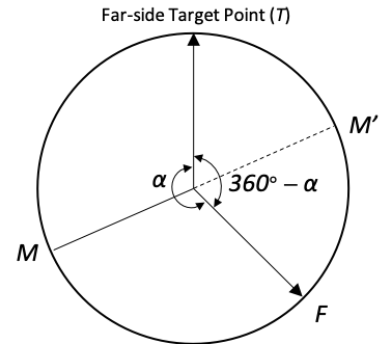


Figure 10 : Mid-point, $\alpha > 180$

3.2.3 Find the 1st and the 2nd In-skip Reflection Points Out of a 3-skip Branch

Similarly, some schemes in Table 1 have a branch with 3 skips, e.g., 3x3-lower, 2x3-upper, etc., Then, for a given far-side target point (T), after a final-skip point (F) is found via exhaustive searching, I have to compute both the 1st and the 2nd in-skip locations between T and F . I use Figure 11 to explain my algorithm.

Suppose there are two points A and B on a great circle that will be split equally into 3 parts, and the center of the circle is O , then based on the angle α formed between vectors \overrightarrow{OA} and \overrightarrow{OB} , i.e., $\angle AOB = \alpha$, I have two cases:

1) Case-1: $\alpha < 180^\circ$

Vectors: $V_1 = \overrightarrow{OA}$, and $V_2 = \overrightarrow{OB}$;

Let Radius = R , then $\|V_1\| = \|V_2\| = R$;

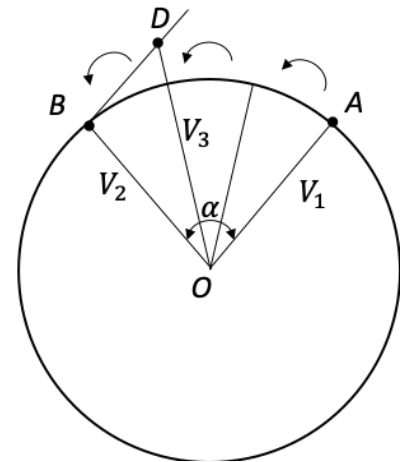


Figure 11 : 3-skip branch, $\alpha < 180$

I draw a line BD, such that $BD \parallel OA$, then I get $\angle AOB + \angle OBD = 180^\circ$. That is, they are supplementary angles. From $\triangle OBD$, the values of the 3 angles $(\angle BOD, \angle BDO, \angle OBD) = \left(\frac{\alpha}{3}, \frac{2}{3}\alpha, 180 - \alpha\right)$, respectively.

Further, let $\overrightarrow{BD} = C \cdot \overrightarrow{OA}$, where C is the parameter I want to compute.

According to the *Law of Sin* in the triangle $\triangle OBD$, $\alpha \neq 0$

$$\left\{ \begin{array}{l} \frac{\|V_2\|}{\sin(\frac{2}{3}\alpha)} = \frac{\|C \cdot V_1\|}{\sin(\frac{1}{3}\alpha)} \\ \|V_1\| = \|V_2\| \end{array} \right\} \Rightarrow \frac{1}{\sin(\frac{2}{3}\alpha)} = \frac{C}{\sin(\frac{1}{3}\alpha)}$$

$$\Rightarrow \frac{1}{2 \cdot \sin(\frac{1}{3}\alpha) \cdot \cos(\frac{1}{3}\alpha)} = \frac{C}{\sin(\frac{1}{3}\alpha)} \Rightarrow C = \frac{1}{2 \cdot \cos(\frac{1}{3}\alpha)}, \text{ Where } \alpha \neq 0, \text{ and } \alpha < 180^\circ$$

Let $V_3 = \overrightarrow{OD}$, then $V_3 = \overrightarrow{OB} + \overrightarrow{BD} = V_2 + C * V_1$. I further normalize to get $V_4 = \frac{V_3}{\|V_3\|}$. Finally, the conversion as in section 3.2.1 will be used to derive the corresponding longitude-sin(latitude) coordinate (λ, θ) .

If the vector V_4 is designated as the 2nd in-skip point, then for the 1st in-skip point, I just need to switch the role of vectors V_1 and V_2 , and apply the above similar algorithm to derive its coordinate. I do not repeat here.

2) Case-2: $\alpha > 180^\circ$

Some schemes in Table 1 have a 3-skip branch whose angle α is greater than 180° . For example, in the 1x3-lower case, the range of the 2nd annulus (for 3-skip branch) is 207.9° to 256.5° . The computation process for this scenario is fairly complicated and I have to dissect it into multiple steps. For the following, T stands for the far-side target point and F is the final-skip location. Please refer to Figure 12 for the algorithm.

Since the angle $\alpha > 180^\circ$, I apply the similar algorithm from the section 3.2.2:case-2 ($\alpha > 180^\circ$), to derive the mid-point M (with the antipode translation);

a) Now, let's consider 2 sets of points (T, M) and (M, F) .

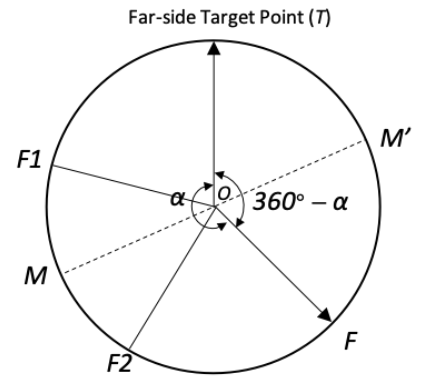


Figure 12 : 3-skip branch, $\alpha > 180$

- i. (T, M): Based on 2D-geometry, I found that the original 1st in-skip point F_1 (relative to T & F) is actually the 2nd reflection location relative to T & M! This is very critical since I can then apply the previous trisecting algorithm to derive the point F_1 . This is because, instead of α , now the angle $\angle TOM$ is $\frac{\alpha}{2}$, which is $< 180^\circ$;
- ii. (M, F): Similarly, the original 2nd in-skip point F_2 (relative to T & F) is actually the 1st reflection location relative to M & F! Then I apply the previous trisecting algorithm to derive the point F_2 , with the angle $\angle MOF = \frac{\alpha}{2}$, which is $< 180^\circ$, of course.

3.2.4 Find the 1st, 2nd, and 3rd In-skip Points Out of a 4-skip Branch

Some schemes in Table 1 have a 4-skip branch, e.g., 2x4-lower, 4x4-upper, etc. Then, for a given far-side target point (T), after a final-skip point (F) is found via exhaustive searching, I could compute all the in-skip reflection points by continuously applying the bisecting algorithm as shown in section 3.2.2. Similarly, there are also two cases depending on the value of angle α formed between vectors \overrightarrow{OT} and \overrightarrow{OF} :

1) Case-1: $\alpha < 180^\circ$

- a) Since $\alpha < 180^\circ$, I can directly apply the algorithm from the section 3.2.2:case-1 ($\alpha < 180^\circ$), to derive the mid-point M_2 as the 2nd in-skip surface reflection;
- b) Now, let's consider 2 sets of points (T, M_2) and (M_2 , F).
 - i. (T, M_2): Now, the angle formed between vectors \overrightarrow{OT} and $\overrightarrow{OM_2}$ is $\frac{\alpha}{2}$, and $\frac{\alpha}{2} < 180^\circ$. Then, I can apply again the same algorithm from section 3.2.2:case-1 ($\alpha < 180^\circ$), to derive the mid-point M_1 as the 1st in-skip surface reflection;
 - ii. (M_2 , F): Similarly, the 3rd in-skip point M_3 is the mid-point of the arc $\widehat{M_2F}$. Then, the same calculation can be done by using $\overrightarrow{OM_2}$ and \overrightarrow{OF} , with the intersecting angle $\frac{\alpha}{2} < 180^\circ$.

2) Case-2: $\alpha > 180^\circ$

- a) Since the angle $\alpha > 180^\circ$, I apply the similar algorithm from the section 3.2.2:case-2 ($\alpha > 180^\circ$), to derive the mid-point M_2 (after the antipode translation). The surface location M_2 is the 2nd in-skip location.
- b) Now, I can consider 2 sets of points (T, M_2) and (M_2 , F).
 - i. (T, M_2): Now, the angle formed between vectors \overrightarrow{OT} and $\overrightarrow{OM_2}$ is $\frac{\alpha}{2}$, and the parameters from Table 1 will guarantee $\frac{\alpha}{2} < 180^\circ$. Then, I can apply the algorithm from the section 3.2.2:case-1 ($\alpha < 180^\circ$), to derive the mid-point M_1 of the arc $\widehat{TM_2}$ as the 1st in-skip surface reflection;

- ii. (M₂, F): Similarly, the 3rd in-skip point M₃ is the mid-point of the arc $\widehat{M_2F}$. Then, the same calculation can be done by using $\overrightarrow{OM_2}$ and \overrightarrow{OF} , with the intersecting angle $\frac{\alpha}{2} < 180^\circ$.

3.2.5 Find the 1st, 2nd, 3rd, 4th, and 5th In-skip Points Out of a 6-skip Branch

There are two schemes in Table 1 having a 6-skip branch, e.g., 2x6-lower, 2x6-upper, etc. Then, for a given far-side target point (T), after a final-skip point (F) is found via exhaustive searching, I can compute all in-skip reflection points by continuously applying the bisecting and trisecting algorithms as shown in sections 3.2.2 and 3.2.3. As previously mentioned, there are also two cases depending on the value of angle α formed between vectors \overrightarrow{OT} and \overrightarrow{OF} :

1) Case-1: $\alpha < 180^\circ$

- a) Since $\alpha < 180^\circ$, I can directly apply the *bisecting* algorithm from the section 3.2.2:case-1 ($\alpha < 180^\circ$), to derive the mid-point M₃ as the 3rd in-skip surface reflection point;
- b) Now, let's consider 2 sets of points (T, M₃) and (M₃, F).
 - i. (T, M₃): Now, the angle formed between vectors \overrightarrow{OT} and $\overrightarrow{OM_3}$ is $\frac{\alpha}{2}$, and $\frac{\alpha}{2} < 180^\circ$. Then, I can apply the *trisecting* algorithm from the section 3.2.3:case-1 ($\alpha < 180^\circ$), to derive the 1st and the 2nd in-skip reflection points;
 - ii. (M₃, F): Similarly, the intersecting angle between vectors $\overrightarrow{OM_3}$ and \overrightarrow{OF} is $\frac{\alpha}{2}$, where $\frac{\alpha}{2} < 180^\circ$. Then, the *trisecting* algorithm from the section 3.2.3:case-1 ($\alpha < 180^\circ$) can also be applied to the arc $\widehat{M_3F}$ to compute the 4th and the 5th in-skip reflection locations.

2) Case-2: $\alpha > 180^\circ$

- a) Since the angle $\alpha > 180^\circ$, I then apply the *bisecting* algorithm from the section 3.2.2:case-2 ($\alpha > 180^\circ$), to derive the mid-point M₃ (after the antipode translation). The surface location M₃ is the 3rd in-skip reflection location;
- b) Now, let's consider 2 sets of points (T, M₃) and (M₃, F).
 - i. (T, M₃): Now, the angle formed between vectors \overrightarrow{OT} and $\overrightarrow{OM_3}$ is $\frac{\alpha}{2}$, and $\frac{\alpha}{2} < 180^\circ$. Then, I can apply the *trisecting* algorithm from the section 3.2.3:case-1 ($\alpha < 180^\circ$), to derive the 1st and the 2nd in-skip reflection points;
 - ii. (M₃, F): Similarly, the intersecting angle between vectors $\overrightarrow{OM_3}$ and \overrightarrow{OF} is $\frac{\alpha}{2}$, where $\frac{\alpha}{2} < 180^\circ$. Then, the *trisecting* algorithm from the section 3.2.3:case-1 ($\alpha < 180^\circ$) can also be applied to the arc $\widehat{M_3F}$ to compute the 4th and the 5th in-skip reflection locations.

Now, I have the algorithms to calculate surface reflection points, including both in-skip and final-skip locations, for all 14 multi-skip schemes. I will analyze the computed data and discuss the physical truth behind them in the next section.

4 Data Inference, Analysis & Discussion

4.1 Hypothetical Causes of the Long-Term Variation of Travel-Time Shifts

I have shown in Figure 3 (in section 1.2) that the average travel-time shift δ_τ has a very good anti-correlation with Sun's magnetic activity. There could be various physical reasons behind it:

1. One possible explanation could be that far-side ARs exhibit themselves as travel-time deficits on the far-side maps; with the waxing and waning of the number of ARs on the far side, one would naturally expect that the far-side δ_τ varies with the solar cycle.
2. Another possible cause could be that far-side maps are calculated using the near-side Dopplergrams [Scherrer et al. 2012, Schou et al. 2012] and it is well known that the Doppler oscillatory signals inside ARs carry travel-time deficits with them. It is thus likely that the travel-time deficits measured in the far-side images come from the deficits in the near-side oscillatory signals used for calculations.
3. The third cause could be a combined effect of the Sun's global ARs, comprised of both far-side and near-side ones. This is because, though the focus might be far-side target-points, the helioseismic waves actually initiate from the near-side and get reflected a few times on different surface locations before converging to that far-side focus, as well as continuing to reflect back to the near-side after leaving that focus point. These surface reflection locations, either on the far-side or near-side, have a probability of residing inside magnetic regions, and travel-time deficits during such surface reflections can be carried along the entire travel of the waves. The more magnetic regions, the more likely surface reflections occur in magnetic regions, and accordingly, more travel-time deficits may be measured in δ_τ .

Actually, the above three causes are not completely independent, and cause-1 and cause-2 are certainly part of cause-3. But, I want to find out here is the **dominant factor** that determines the variation trend of the averaged deficit δ_τ .

4.2 Cause#1: Dominated by Far-side ARs?

I plot in the Figure 13 the long-term evolution of the Sun's magnetic fields $|B|$ obtained from the near-side full disk as well as from the near-side northern and southern hemisphere. Because $|B|$ is averaged over a 90-day period, the mean far-side magnetic-flux density is not expected to differ much from that of the near side. Here, the three curves in the figure are showing different trends.

If cause#1 dominates, one would expect naturally that δ_τ shows a different trend that should be commensurate with the magnetic fields of the northern and southern hemispheres, respectively. However, when I compare them to the long-term variation of δ_τ in Figure 2 (in section 1.2), their non-matching trends clearly demonstrate that the cause#1 is **not** the dominant reason.

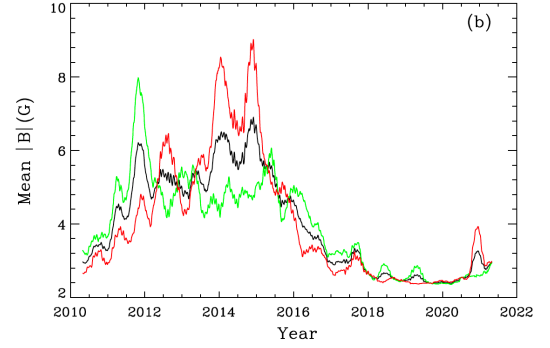


Figure 13 : Long-term evolution of the Sun's near-side magnetic fields $|B|$ (Black: full-disk; Green: Northern-hemisphere; Red: Southern-hemisphere).

4.3 Cause#2: Dominated by Near-side Dopplergrams?

In order to examine if the near-side oscillatory signals stand the dominant factor, I analyze my computational results obtained based on the time-distance far-side imaging technique.

4.3.1 Mean Travel-Time Shifts & Number of Skips:

The time-distance far-side imaging technique has the advantage of having multiple multi-skip measurements that provide more data to track down the causes of the general variation trend of δ_τ . Comparing δ_τ measured from different measurement schemes, i.e., different combinations of wave-skips, may shed a light on how to understand the δ_τ variation with the solar cycle.

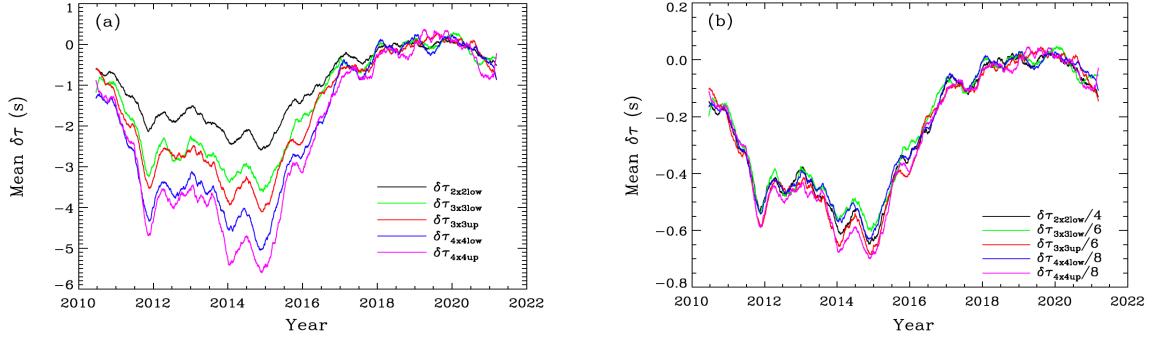


Figure 14 : (a) Temporal evolution of $\delta\tau$ measured from the far-side central area using the measurement schemes of 2x2-lower, 3x3-lower, 3x3-upper, 4x4-lower, and 4x4-upper; (b) shows $\delta\tau / N$, where N is the number of skips in the corresponding measurements.

Figure 14(a) shows the temporal evolution of $\delta\tau$ measured from the far-side central area using the measurement schemes of 2x2-lower, 3x3-lower, 3x3-upper, 4x4-lower, and 4x4-upper; and Figure 14(b) shows $\delta\tau / N$, the $\delta\tau$ divided by their respective number of skips used in the measurements. As can be seen, the $\delta\tau$ from different measurement schemes show substantial differences in values although all of them show a very similar general trend of variations with the solar cycle. However, the $\delta\tau / N$ are essentially consistent with each other, indicating that a single skip from each measurement scheme gets similar amounts of travel-time reduction.

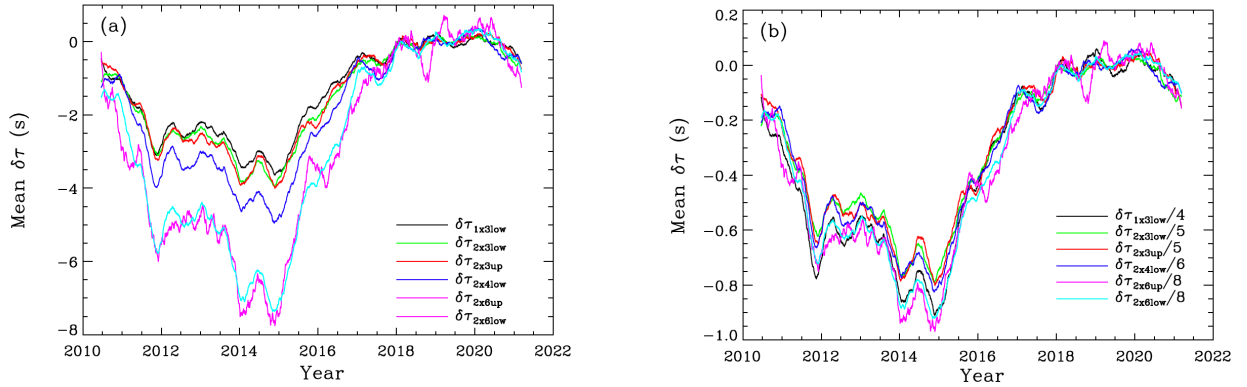


Figure 15 : (a) shows $\delta\tau$ and (b) shows $\delta\tau / N$ measured from the far-side limb areas

Similarly, Figure 15(a) & (b) shows $\delta\tau$ and $\delta\tau / N$ measured from the limb areas of the far side, including the measurement schemes of 1x3-lower, 2x3-lower, 2x3-upper, 2x4-lower, 2x6-upper, and 2x6-lower, respectively. Not much deviation from the results of the far-side central region, the $\delta\tau$ from different measurement schemes differ substantially, though $\delta\tau / N$ are quite consistent with each other, with a relatively nonnegligible differences compared to the central-area schemes.

4.3.2 Data Inference: Cause#2 Not Dominant

I presume for cause#2 that the travel-time deficits measured in the far-side images come from the deficits in the near-side oscillatory signals. Therefore, if cause#2 is the dominant factor, then one would expect that the δ_τ with a different number of wave skips shall show a similar amount of variations because essentially similar near-side oscillatory signals are used in all of these calculations. However, both Figure 14(a) and Figure 15(a) show the other way around. Thus, I can also rule out the dominant impact of the cause#2.

4.4 Cause#3: A Combined Effect of the Sun's Global Active Regions?

4.4.1 Data Inference: Mean Travel-Time Shifts & Latitude-Bands:

To investigate if the dominant factor of the long-term variation is a combined effect of the magnetic fields distributed around the global Sun, including both the northern and the southern hemisphere, I first assess the relationship between the δ_τ measurement and the Sun's latitude.

Figure 16 shows the variation trends of the δ_τ , obtained from a few selected latitudinal bands in the combined far-side images (from all 14 schemes in Table 1, rather than images of different measurement schemes), with Figure 16(a) covering the northern hemisphere and Figure 16(b) covering the southern hemisphere, respectively. Although their general trends are very similar, the values of the δ_τ actually differ from each other significantly. The δ_τ in the lower latitude bands have greater magnitudes than those in the higher latitude bands, which is commensurate with the non-uniform distribution of the Sun's whole magnetic fields, i.e., weaker field in the high-latitude areas compared to greater magnitude in the low-latitude areas. These results indicate that although the general trend of the δ_τ variation seems to be caused by a global factor, the variations are actually latitude dependent.

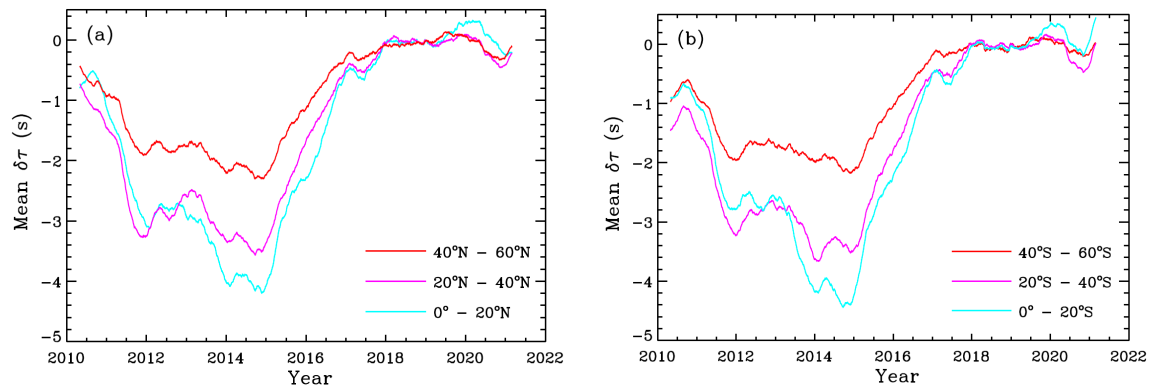


Figure 16 : Temporal variations of far-side $\delta\tau$ for selected latitudinal bands in the (a) northern and (b) southern hemispheres.

4.4.2 Influence of Sun's Global Magnetic Field

It is known that, wherever magnetic fields are present at the reflection locations, travel-time deficits may be introduced in the measurements of far-side δ_τ . Therefore, to explore the impact of the Sun's whole magnetic field, I need to examine the probability of acoustic (i.e., helioseismic) waves, which carry far-side information back to the near side, encountering magnetic regions on the solar surface during their journey.

Helioseismic waves that are used to map far-side ARs often experience a few surface reflections during their travels through the globe. For example, Figure 1 shows the 1x3-lower scheme in which a helioseismic wave initiates from the near-side and touch the solar surface five times during the whole process. Obviously, though far-side target points in my model may reside in an $120^\circ \times 180^\circ$ (latitude x longitude) area on Sun's far-side, the reflection points of waves are actually distributed over most of the Sun's latitudes. In fact, as explained in section-3, for one measurement scheme and for one far-side target point, there are hundreds of thousands of associated surface reflection points even with a low spatial-resolution of $0.8^\circ \times 0.8^\circ \text{ pixel}^{-1}$, and the volume is even larger considering the different skip-distances that fall into the annuli's ranges as shown in Table 1. Further, remember that there are 14 δ_τ measurements from 14 schemes for each far-side target point.

The surface reflection locations are computed separately for each measurement scheme through the spherical geometry algorithms as in section-3. Because the eventually measured δ_τ depends on the latitudinal distribution of these reflection locations, and the large number of reflections differ greatly for different latitude bands, therefore, it makes sense to bin down the number of reflection locations into different latitudinal bands and only consider the probability density function of the reflection locations in each band.

The total number of reflections are counted for each 5° -wide latitudinal band from -90° to $+90^\circ$. So, I have totally 36 bands, with the latitudinal band-index, λ , as an integer in the range $[0, 35]^2$. I define the

² In section 3.1.1, I did specify that the latitude of a far-side target point in my model is only within the range $[-60^\circ, +60^\circ]$. However, please note that my computation will generate *in-skip* surface reflection points whose latitude values might fall in the whole range of $[-90^\circ, +90^\circ]$. That is why I define latitudinal bands over the full latitude range.

probability density function $pdf(\lambda)$ by normalizing the number of reflections in each band relative to the total number of reflections across all bands:

$$pdf(\lambda) = \frac{N(\lambda)}{\sum_{\lambda=0}^{35} N(\lambda)}, \lambda \in Z \text{ and } \lambda = [0..35],$$

where $N(\lambda)$ is the number of surface reflection points in the latitudinal band as indexed by λ .

I then define $|B(\lambda)|$ as the daily average of absolute values of the full-disk magnetic field over the same 5°-wide latitudinal bands, and then calculate an averaged magnetic-field strength at all the wave's reflection locations, i.e., adjusted probabilistically by $pdf(\lambda)$ as:

$$\langle |B(\lambda)| \rangle = pdf(\lambda) * |B(\lambda)|, \lambda \in Z \text{ and } \lambda = [0..35]$$

Here $\langle |B(\lambda)| \rangle$ indicates the averaged magnetic-field strength, in a latitudinal band-index λ , the waves encounter on the surface along their entire journey from the near side to the far side and then back to the near side. These $\langle |B(\lambda)| \rangle$ are then averaged into 20°-wide latitudinal bands, i.e., combining four 5°-wide bands, for each day to compare against the δ_τ measurements as shown in Figure 16. Figure 17 shows the results after a 180-day running average. Note that values of δ_τ are marked on the right of the figure.

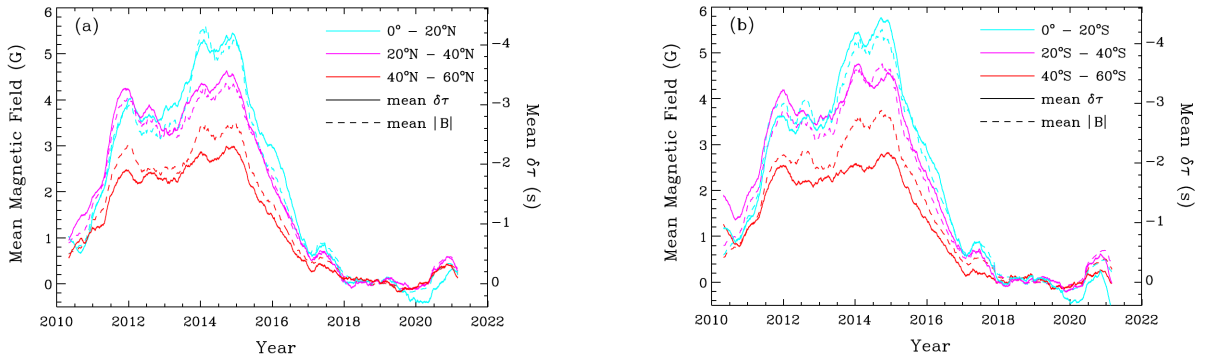


Figure 17 : Temporal variations of far-side $\delta\tau$ (solid lines), plotted decreasing upward, and $\langle |B(\lambda)| \rangle$ (dashed lines) for selected latitudinal bands in both (a) northern and (b) southern hemispheres.

For the latitudinal bands of 0° ~ 20° and 20° ~ 40° in both hemispheres, the trend and values of δ_τ and $\langle |B(\lambda)| \rangle$ match pretty well, implying there is a single scaling factor between these two quantities. However, the δ_τ in the 40° ~ 60° band are noticeably smaller than $\langle |B(\lambda)| \rangle$ with that same scaling factor.

4.4.3 Data Inference: Cause#3 is Dominating

We thus believe that, conforming to cause#3, the long-term variation of δ_τ is caused collectively by the magnetic fields distributed around the global Sun, whose interactions with the traveling acoustic waves at their surface reflection locations around the globe leave a travel-time deficit on the far-side acoustic maps.

5 Conclusion & Further Consideration:

The time-distance far-side images from 11 years of SDO/HMI observations exhibit a long-term variation in the disk-averaged travel-time shifts δ_τ , which demonstrate a very good anti-correlation with the near-side magnetic flux density, averaged over a running 90-day period, that varies with the solar cycle. The multiple multi-skip measurement schemes that are used to image the far side of the Sun allow me to analyze the single-skip travel-time deficits and the travel-time deficits measured in different latitudinal bands. Over the three hypothetical causes that might have dominated the long-term variation of δ_τ , i.e., the far-side ARs, the near-side oscillatory signals, and the Sun's global magnetic fields, my computational results and data analysis demonstrate that the long-term variation in the far-side travel-time shift is *primarily* caused, collectively, by the surface reflections which unavoidably interact with the magnetic fields (or ARs) that are distributed non-uniformly around the Sun.

Toward the end of this paper, I want to mention another work by Gonzalez et al. [2009], in which they found that the mean helioseismic phase-shifts, deficits of which indicate far-side ARs, varied substantially with the phase of the solar cycle. However, they attributed the long-term phase-shift variation to the Sun's seismic radius change with solar cycles. While I conclude that the dominant factor that has led to the long-term variation of the measured far-side travel-time shift is the effect of the Sun's global ARs, my analysis does not exclude the possible impact of the seismic radius of the Sun, though I don't think it is the dominant factor. More detailed comparisons and analytic results can be found in my co-authored paper [Zhao, Jiang, Chen, 2021].

Acknowledgements: The results in this paper are achieved under the guidance of Dr. Junwei Zhao and Dr. Ruizhu Chen of Stanford University. Their patience and constructive advice help me smoothly start, develop, and finally conclude all of my work. Further, part of the work presented here has been included in the paper [Zhao, Jiang, Chen, 2021] for publication in the *Journal of Solar Physics* (currently under review).

Bibliography:

- Braun, D.C., Lindsey, C.: 2001, *Astrophys. J. Lett.* 560, L189
- Gonzalez Hernandez, I., Scherrer, P., Hill, F.: 2009, *Astrophys. J. Lett.* 691, L87
- Hartlep, T., Zhao, J., Mansour, N.N., Kosovichev, A.G.: 2008, *Astrophys. J.*, 689, 1373
- Ilonidis, S., Zhao, J., Hartlep, T.: 2009, *Solar Phys.* 258, 181
- Kholikov, S., Hill, F.: 2008, *Solar Phys.* 251, 157
- Kosovichev, A., Rozelot, J.-P.: 2018, *Astrophys. J.* 861, 90
- Lefebvre, S., Kosovichev, A.G.: 2005, *Astrophys. J. Lett.* 633, L149
- Lindsey, C., Braun, D.C.: 2000, *Science* 287, 1799
- Lindsey, C., Braun, D.C.: 2017, *Space Weather* 15, 761
- Lindsey, C., Cally, P.S., Rempel, M.: 2010, *Astrophys. J.* 719, 1144
- Scherrer P.H., Bogart R.S., Bush R.I., et al.: 1995, *Solar Phys.* 162, 129
- Scherrer, P.H., Schou, J., Bush R.I., et al.: 2012, *Solar Phys.* 275, 207
- Schrijver, C. J., & DeRosa, M. L. 2003, *SoPh*, 212, 165
- Schou J., Kosovichev A.G., Goode P.R., Dziembowski W.A.: 1997, *Astrophys. J. Lett.*, 489, L197
- Schou, J., Scherrer, P.H., Bush R.I., et al.: 2012, *Solar Phys.* 275, 229
- Upton, L., & Hathaway, D. H. 2014, *ApJ*, 780, 5
- Zhao, J.: 2007, *Astrophys. J. Lett.* 664, L139
- Zhao, J., Hing, D., Chen, R., Hess Webber, S.: 2019, *Astrophys. J.*, 887, 216
- Zhao, J., Jiang, G., Chen, R.: 2021, submitted to *Journal of Solar Physics* (currently under review).
- NASA SDO: <https://sdo.gsfc.nasa.gov/mission/instruments.php>
- NASA SDO/HMI Doppler observations: <https://www.nasa.gov/content/goddard/sdo-hmi-dopplergram/>
- Stanford JSOC: <http://jsoc.stanford.edu/data/timed/>